Gap junctions mediate large-scale Turing structures in a mean-field cortex driven by subcortical noise

Moira L. Steyn-Ross,[1,*] D. A. Steyn-Ross,[1] M. T. Wilson,[1] and J. W. Sleigh[2]
[1]*Department of Engineering, Private Bag 3105, University of Waikato, Hamilton 3240, New Zealand*
[2]*Waikato Clinical School, University of Auckland, Waikato Hospital, Hamilton 3204, New Zealand*
(Received 15 February 2007; revised manuscript received 18 April 2007; published 24 July 2007)

One of the grand puzzles in neuroscience is establishing the link between cognition and the disparate patterns of spontaneous and task-induced brain activity that can be measured clinically using a wide range of detection modalities such as scalp electrodes and imaging tomography. High-level brain function is not a single-neuron property, yet emerges as a cooperative phenomenon of multiply-interacting *populations* of neurons. Therefore a fruitful modeling approach is to picture the cerebral cortex as a continuum characterized by parameters that have been averaged over a small volume of cortical tissue. Such mean-field cortical models have been used to investigate gross patterns of brain behavior such as anesthesia, the cycles of natural sleep, memory and erasure in slow-wave sleep, and epilepsy. There is persuasive and accumulating evidence that direct gap-junction connections between inhibitory neurons promote synchronous oscillatory behavior both locally and across distances of some centimeters, but, to date, continuum models have ignored gap-junction connectivity. In this paper we employ simple mean-field arguments to derive an expression for D_2, the diffusive coupling strength arising from gap-junction connections between inhibitory neurons. Using recent neurophysiological measurements reported by Fukuda *et al.* [J. Neurosci. **26**, 3434 (2006)], we estimate an upper limit of $D_2 \approx 0.6$ cm^2. We apply a linear stability analysis to a standard mean-field cortical model, augmented with gap-junction diffusion, and find this value for the diffusive coupling strength to be close to the critical value required to destabilize the homogeneous steady state. Computer simulations demonstrate that larger values of D_2 cause the noise-driven model cortex to spontaneously crystalize into random mazelike Turing structures: centimeter-scale spatial patterns in which regions of high-firing activity are intermixed with regions of low-firing activity. These structures are consistent with the spatial variations in brain activity patterns detected with the BOLD (blood oxygen–level–dependent) signal detected with magnetic resonance imaging, and may provide a natural substrate for synchronous gamma-band rhythms observed across separated EEG (electroencephalogram) electrodes.

DOI: 10.1103/PhysRevE.76.011916 PACS number(s): 87.19.La, 05.70.Fh, 87.17.Aa, 87.18.Hf

I. INTRODUCTION

It is generally believed that cognition—the conscious process by which individuals perceive, think, and remember—requires the simultaneous and temporary activation of distinct regions of the cerebral cortex, linked for sufficient time to allow "binding" of a cohesive mental picture [1]. Consequently, understanding the temporal and spatial patterns of brain activity is of central interest to the neuroscience and cortical modeling communities. In this paper we will propose a mechanism for the spontaneous emergence of spatial patterning in the cortex arising from gap-junction diffusion between inhibitory neurons.

The number of neurons in the cortex is immense, so, rather than attempting to follow discrete neuron-by-neuron interactions, it is natural for cortical modelers to treat the cortex as a continuum of excitable tissue. Following earlier researchers [2–5], we adopt a mean-field approach which assumes that neural parameters have been averaged over a small volume of cortical gray matter. In recent papers we have used this mean-field approach to investigate the bulk electrodynamic properties of the cortex during induction of, and recovery from, drug-induced anesthesia [6–9], during the cycles of natural sleep [10–12], and proposed a memory and erasure function for slow-wave sleep [13]. Other workers have applied continuum models to the propagation and stability of cortical waves [4,14], gamma-band oscillations [5,15], EEG spectral prediction [16], anesthesia [17], and epilepsy [18,19].

Until now, all continuum models have assumed that communication between neurons is exclusively via *chemical* synapses; in fact, neurons can also communicate via direct *electrical* synapses, also known as *gap junctions*. The existence of gap junctions in the mammalian brain has been known for decades, but only recently has their electrophysiological significance been realized (for review, see Bennett and Zukin [20]). It is now known that adjacent neurons coupled directly by electrical synapses will tend to synchronize their firing behavior [21–25]. The recent finding that gap junctions among dendrites of inhibitory cortical neurons establish dense and widespread networks that can be traced in a boundless chain [26] gives strong support to the notion that electrical diffusion via gap junctions permits not only short-range local synchrony, but also long-range synchronized oscillations extending across the cortex. These findings motivate us to introduce a simple mean-field treatment of gap-junction connectivity, allowing us to augment the continuum equations described in our earlier work [7,11] by incorporat-

*msr@waikato.ac.nz; URL: phys.waikato.ac.nz/cortex

ing the diffusive effects of copious gap contacts between neurons.

The plan of the paper is as follows. In Sec. II A we offer a simple continuum treatment for gap-junction connections. We define the grain size, a, of our diffusion lattice to be the area of diffusive sensitivity for a single neuron, and estimate the size of the coupling resistance between lattice cells from the measurements of Fukuda *et al.* [26]. We allow the gap-junction diffusion currents to integrate at the membrane soma, and hence derive an expression for D_2, the diffusive coupling strength for inhibitory neurons. We find that D_2 is directly proportional to lattice-cell area, a, and to the ratio of membrane resistance to gap resistance, R_m/R_g. This direct derivation for D_2 is supplemented in the Appendixes by a pair of alternative derivations that assume that gap-junction connectivity is (a) Gaussian-distributed about an origin (Appendix A) or (b) proportional to the overlap area between two Heaviside-weighted disks (Appendix B). Although these alternative approaches give smaller estimates for D_2, we find that both derivations give a mathematical form which has precisely the same dependence on effective grain size and resistance ratio as that obtained using the simple analysis.

The relevant stochastic DEs for the cortex, under the control of variable subcortical driving ϕ_e^{sc}, are given in Sec. II B. The diffusive effects of gap junctions enter the time-evolution equations for soma voltages in the form of Laplacians scaled by excitatory and inhibitory diffusion coefficients D_1, D_2, respectively.

Section II C examines the homogeneous steady-state behavior of the cortex. We find that, over an intermediate range of subcortical drive, the locus of equilibrium states exhibits a multiple-root region for the state variables V_e (excitatory soma voltage) and Q_e (excitatory firing rate); this is illustrated in Fig. 3. Linear stability analysis shows that, in the absence of gap junctions, the upper and lower branches are stable with respect to small spatio-temporal perturbations, whereas the middle branch is unstable. When gap junctions are included, the stability picture changes: The previously stable upper and lower branches are predicted to become unstable for a range of spatial frequencies, with the degree of instability increasing strongly with increases in inhibitory diffusion. Thus strong inhibitory diffusion will cause perturbations to grow, breaking the homogeneous symmetry and replacing it with a spatially patterned structure.

To investigate the form of the patterns, in Sec. III B we simulate the nonlinear stochastic equations on a grid, driving the cortex with small-amplitude spatiotemporal white noise. When diffusion is present, we find that the cortex spontaneously organizes itself into random mazelike linked structures containing regions of high cortical activity intermixed with regions of low activity. These are Turing patterns, named for Turing's seminal work [27] proposing chemical morphogenisis as a basis for pattern formation in biology. We find the Turing instability to be a remarkably robust feature of the gap-junction-mediated cortex, and is not critically dependent on the level of subcortical stimulation or initial conditions.

In the Discussion (Sec. IV) we highlight the correspondence between the cortical system of interacting excitatory and inhibitory nerve cells and the classical reaction-diffusion chemical system of interacting activator and inhibitor morphogens. The fact that gap junctions between interneurons vastly outnumber those between excitatory neurons means that the inhibitory diffusion in the cortex is stronger than excitatory diffusion: $D_2 > D_1$. This mismatch corresponds to the Turing instability requirement for a chemical reactor—namely, that the inhibiting agent diffuse more rapidly than the activator [28,29]. We argue that the remote coactivation of separated cortical regions is consistent with the spatial variations in brain activity patterns detected with the BOLD (blood oxygen-level-dependent) signal using magnetic resonance imaging [30–32]. Further, we observe that since D_2 is directly proportional to soma membrane resistance, elevated firing rates are likely to reduce coupling strength, leading to slow fluctuations in Turing contrast. We conclude by suggesting that diffusion-induced Turing structures would provide a natural substrate for the transient gamma-band synchronies that have been reported by many researchers [33–37].

II. THEORY

A. Mean-field treatment of gap junctions

Gap junctions, also known as electrical synapses, are clusters of protein channels that connect the interiors of adjoining neurons, allowing direct exchange of electric charge (largely K^+) and intracellular signaling molecules [20]. They are thought to play an important role in morphogenesis, pattern formation, and brain development. Electrophysiological measurements [21,22,26] show that these between-cell connections obey Ohm's law, with a current flow proportional to the voltage difference, $\Delta V=(V-V')$, between joined cells,

$$I_{\text{gap}} = g(V - V'). \tag{1}$$

Measured values for gap-junction conductance (inverse resistance) g depend on cell size and type, with quoted values typically in the range 0.3 to 7 nS, corresponding to a single-channel gap resistance ranging from 3 GΩ down to 140 MΩ.

It is clear from Eq. (1) that the gap current between coupled neurons can only disappear when the voltage difference $(V-V')$ between those nerve cells is zero, i.e., when the neuron pair is perfectly synchronized with identical membrane voltages. Therefore, the presence of gap currents will tend to synchronize neuron behaviors, not only during subthreshold fluctuations but also during periods of active firing. Synchronized behavior has been observed in whole-cell recordings of gap-junction-connected inhibitory neurons (GABAergic interneurons) in the neocortex [23,24], and confirmed in realistic conductance-based computer models [25].

To date, theoretical modeling of gap-junction effects has been confined to detailed neuron-by-neuron simulations, and there has been little motivation to develop a mean-field continuum theory for gap junctions. This situation is changing now that the true extent of gap-junction coupling is becoming apparent. Fukuda *et al.* [26] present clear experimental evidence for gap junctions that are not restricted to proximal dendrites, but occur at distances up to 380 μm from the cell body (soma). Within a cylinder of cortical tissue (containing

layers 2 and 3 of cat visual cortex; tangential surface area 1 mm^2), Fukuda *et al.* counted ~400 large (*L*-type) interneurons, with each neuron making an average of 60±12 (mean±SD) gap junction connections with both proximal and distal neurons of the same type. They found that serially interconnected neurons could be traced laterally in a boundless manner through multiple gap junctions on their dendritic trees, thereby forming an extended, dense, and relatively homogeneous network that extended across multiple orientation-preference columns of the visual cortex. The substantial overlap between dendritic fields is illustrated in Fig. 1.

We wish to develop a simple continuum model for dense gap-junction connectivity, then incorporate this into an established mean-field cortical model that includes standard chemical-synapse connections and stochastic subcortical driving. By "mean field," we imply a deliberate spatial blurring of detailed physiology in order to bring out the gross behaviors of cooperating *populations* of neurons that should be detectable with cortical or scalp electrodes. Thus we will make use of soma voltages that have been averaged over the *N* neurons within a small volume of cortical tissue, and express axosynaptic and gap-junction connectivities on a *per neuron* basis.

Suppose there is a momentary voltage perturbation at some point within a population of gap-coupled neurons. The perturbation will propagate outwards via an Ohmic diffusive process. We need to estimate *a*, the characteristic "diffusion grain size" that takes account of the area of *diffusive influence* (identical to the area of *diffusive sensitivity*, since gap connections are symmetric) of the dendritic tree belonging to a single neuron. This grain size *a* defines the area of our unit diffusion cell. We will use the measurements of Fukuda *et al.* [26] to estimate *a* for *L*-type inhibitory neurons.

1. Area of Fukuda diffusion cell

Fukuda's Fig. 5B shows that, for a single neuron, the number of gap junctions per unit length of dendrite is nearly constant, only weakly decaying with distance. Although in one case, gap-junction connectivity was measured to extend out as far as 380 μm from the soma, most dendrites had shorter lengths, and ~98% of gap junctions occurred at distances less than 200 μm from the soma. As a first approximation, we will assume that all gap junctions along the dendrite contribute equally and that the maximum radial extent of gap-junction sensitivity is 200 μm. Thus the zone of diffusive sensitivity for an *L*-type neuron is bounded by a circle of radius ~200 μm; see Fig. 1(b). In Fig. 1(c) we circumscribe the circular zone with a square of side 0.4 mm and area $a=0.16$ mm^2. We will refer to this square zone as the "Fukuda diffusion cell," and picture the population of cortical interneurons as supporting a diffusive latticework of such Fukuda cells.

2. Diffusion-cell coupling resistance

We can also use the Fukuda paper to estimate *R*, the effective coupling resistance between neighboring diffusion cells. Interneurons are distributed randomly across the plane

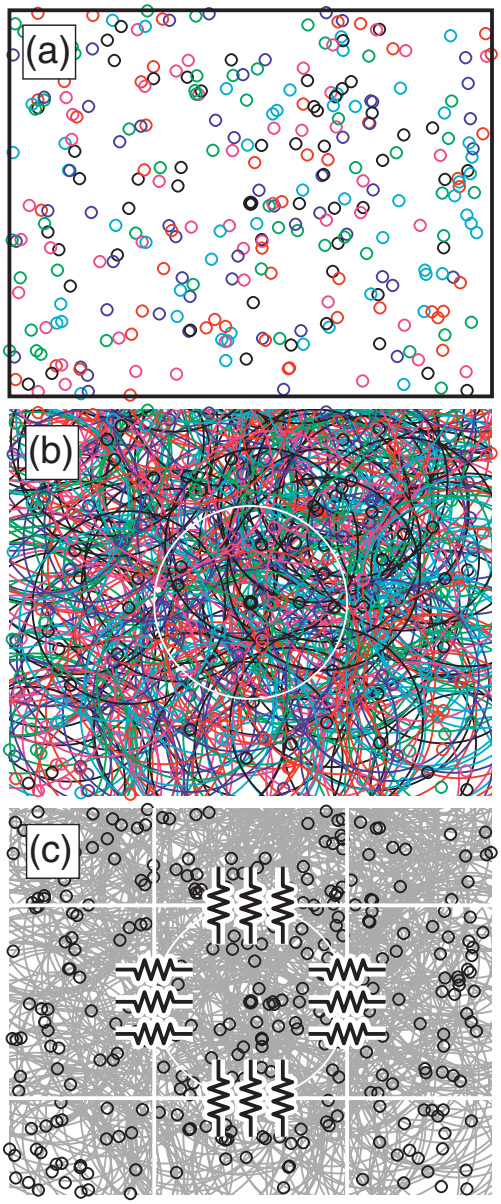

FIG. 1. (Color) Mapping gap-coupled interneurons in the cortex to a mean-field lattice of diffusion cells. (a) Random distribution of inhibitory neurons for a 1-mm × 0.8-mm slice of visual cortex, using measurement statistics reported by Fukuda *et al.* [26] for cat visual cortex. The neuron number density is 400 mm^{-2}; the neuron placements were determined here by sampling a uniform random-number generator. (b) Each neuron is surrounded by a circle of radius 0.2 mm to represent the areal zone of influence from gap-junction contacts on the neuron's dendritic tree. Each interneuron makes ~60 gap-junction contacts with surrounding interneurons at distances up to 0.38 mm; about 98% of contacts occur within the 0.2-mm radius. [Modified from Fig. 9(b) of Fukuda *et al.*; here, the colors are used to aid separation of the rings, and have no physical significance.] (c) We define our lattice diffusion-cell ("Fukuda cell") as the square region that circumscribes the 0.2-mm circle centered on the neuron of interest (small black circle in middle of the figure). The resistors crossing each edge represent the parallel resistive couplings between Fukuda cells arising from multiple gap-junction contacts.

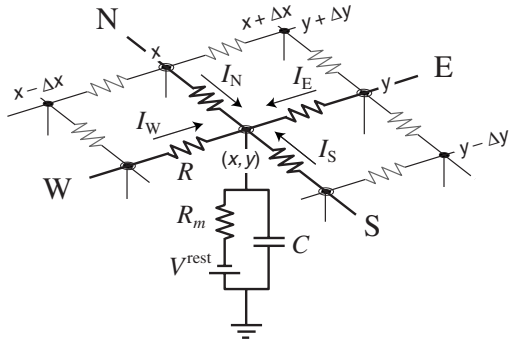

FIG. 2. Cortex modeled as a 2D rectangular network of diffusively-coupled neurons. Each neuron is represented as an *RC* integrator of membrane resistance R_m and capacitance C, charged by a battery of voltage V^{rest}, the cell's resting potential. The neuron at node (x,y) is at the center of its Fukuda diffusion cell (zone of diffusive sensitivity) of area $a=(\Delta x)^2=(\Delta y)^2$. The neuron receives *diffusive* currents from the four neighboring diffusion cells whose centers are labeled N, S, W, E. (Note that *synaptic* input currents are not shown.)

[see Fig. 1(a)], so the connectivity of a given neuron cannot depend in any way on its location relative to a lattice boundary. In particular, a neuron sitting next to the lattice edge must have the same gap-junction connectivity as a neuron at the center of the lattice cell, namely: 15 parallel gap resistances in each of the four compass directions (N, S, W, E), for a total of 60 gap-resistance junctions. Therefore, the *per neuron* coupling resistance, R, between adjacent Fukuda cells will be one-fifteenth of the single-junction resistance,

$$R = \frac{R_g}{\frac{1}{4}N_{ii}^{\gamma}}, \tag{2}$$

where $N_{ii}^{\gamma}=60$ is the per-neuron i-to-i (inhibitory-to-inhibitory) count of gap-junction connections, and R_g is the resistance of a connexin-36 gap junction. Fukuda *et al.* remark that small gap junctions, and gap junctions based on non-connexin-36 proteins, would have gone undetected in their analysis. Thus both the area of diffusivity sensitivity, a, and gap-connectivity per neuron, N_{ii}^{γ}, could well need to be revised upward.

3. Soma integration of gap currents

Consider a square network of Fig. 1(c)–style Fukuda diffusion cells interconnected, in a nearest-neighbor scheme, by coupling resistances R. The neuron at the center of Fig. 2 receives four diffusion currents from the neighboring diffusion cells whose centers are located at nodes labeled N, S, W, E. These currents are integrated at the neuron soma with a time constant $\tau=R_mC$, where C is the membrane capacitance and R_m is the membrane resistance. In the absence of input currents, the neuron voltage V relaxes toward a resting voltage V^{rest}, represented in Fig. 2 as a battery, of magnitude V^{rest}, in series with the membrane resistance, and oriented to give a membrane voltage that is negative relative to the zero potential (indicated with a ground symbol) defined by the extracellular ionic fluid.

The total current to ground is the membrane current $(V-V^{\text{rest}})/R_m$, plus the current through the capacitance, CdV/dt. This total current must match the sum of the synaptic input currents I_{syn} (generated by action potentials incident at the dendrite; not shown in Fig. 2) plus gap-junction diffusive currents I_{gap},

$$(V-V^{\text{rest}})/R_m + C\frac{dV}{dt} = I_{\text{syn}} + I_{\text{gap}}, \tag{3}$$

where

$$I_{\text{gap}} = I_{\text{E}} + I_{\text{W}} + I_{\text{N}} + I_{\text{S}}. \tag{4}$$

Applying Ohm's law, the gap currents entering (x,y) from nodes E and W are, respectively,

$$I_{\text{E}} = \frac{1}{R}[V(x+\Delta x,y) - V(x,y)], \tag{5a}$$

$$I_{\text{W}} = \frac{1}{R}[V(x-\Delta x,y) - V(x,y)], \tag{5b}$$

giving

$$I_{\text{E}} + I_{\text{W}} = \frac{(\Delta x)^2}{R}\left[\frac{V(x+\Delta x,y) - 2V(x,y) + V(x-\Delta x,y)}{(\Delta x)^2}\right] \approx \frac{(\Delta x)^2}{R}\frac{\partial^2 V}{\partial x^2}. \tag{6}$$

Similarly for the gap currents entering from the N and S nodes,

$$I_{\text{N}} + I_{\text{S}} = \frac{(\Delta y)^2}{R}\left[\frac{V(x,y+\Delta y) - 2V(x,y) + V(x,y-\Delta y)}{(\Delta y)^2}\right] \approx \frac{(\Delta y)^2}{R}\frac{\partial^2 V}{\partial y^2}. \tag{7}$$

Adding Eqs. (6) and (7) gives the total gap current entering the neuron at (x,y),

$$I_{\text{gap}} \approx \frac{a}{R}\left[\frac{\partial^2 V}{\partial x^2} + \frac{\partial^2 V}{\partial y^2}\right] \equiv \frac{a}{R}\nabla^2 V. \tag{8}$$

We have written $(\Delta x)^2=(\Delta y)^2=a$, the area of the Fukuda diffusion cell. The Taylor-series expansion to second-order implied by Eqs. (6) and (7) should be valid provided that the length of the Fukuda cell is much smaller than the distances over which the average soma voltage is expected to vary significantly. This is certainly the case for the Turing patterns of Figs. 5 and 6, for which the voltage variations occur on spatial scales of several centimeters, i.e., about two orders of magnitude larger than the dimension of the Fukuda cell.

If only diffusion currents enter the soma (i.e., $I_{\text{syn}}=0$), then substituting Eq. (8) into Eq. (3) gives,

$$(V-V^{\text{rest}})/R_m + C\frac{\partial V}{dt} = \frac{a}{R}\nabla^2 V. \tag{9}$$

Multiplying both sides of Eq. (9) by membrane resistance $R_m=\tau/C$, and substituting the effective Fukuda resistance R

TABLE I. Standard values for the neural model. Subscript label k means destination cell can be either of type e (excitatory) or i (inhibitory).

Symbol	Description	Value	Unit
$\tau_{e,i}$	membrane time constant	0.040, 0.040	s
$V_{e,i}^{\mathrm{rev}}$	reversal potential at dendrite	0, −70	mV
$V_{e,i}^{\mathrm{rest}}$	cell resting potential	−64, −64	mV
$\rho_{e,i}$	synaptic gain at resting voltage	$(1.00, -1.134)\times 10^{-3}$	mV·s
γ_{ek}	rate constant for $e\rightarrow k$ synaptic input	70	s^{-1}
γ_{ik}	rate constant for $i\rightarrow k$ synaptic input	58.6	s^{-1}
N_{ek}^{α}	long-range $e\rightarrow k$ axonal connectivity	3710	
N_{ek}^{β}	local $e\rightarrow k$ axonal connectivity	410	
N_{ik}^{β}	local $i\rightarrow k$ axonal connectivity	800	
N_{ii}^{γ}	$i\leftrightarrow i$ gap-junction connectivity	60	
$\langle\phi_{ek}^{\mathrm{sc}}\rangle$	mean level of $e\rightarrow k$ subcortical synaptic flux	375	s^{-1}
v	axonal conduction speed	140	$\mathrm{cm\,s}^{-1}$
Λ_{ek}	inverse-length scale for $e\rightarrow k$ axonal connections	4	cm^{-1}
$Q_{e,i}^{\max}$	maximum firing rate	30, 60	s^{-1}
$\theta_{e,i}$	sigmoid threshold voltage	−58.5, −58.5	mV
$\sigma_{e,i}$	standard deviation for threshold	4, 6	mV
a	area of Fukuda diffusion cell	0.16	mm^2
$L_{x,y}$	length and width of cortical sheet	25, 25	cm

from Eq. (2), gives a differential equation for the time course of the neuron voltage when driven by diffusive currents,

$$(V - V^{\mathrm{rest}}) + \tau\frac{\partial V}{dt} = \frac{aN_{ii}^{\gamma}}{4}\frac{R_m}{R_g}\nabla^2 V = D_2\nabla^2 V, \qquad (10)$$

where we have defined D_2,

$$D_2 \equiv \frac{aN_{ii}^{\gamma}}{4}\frac{R_m}{R_g}, \qquad (11)$$

the diffusive coupling strength for *inhibitory* neurons (we reserve the symbol D_1 for the corresponding, but much weaker, *excitatory* diffusive coupling strength; this aspect is discussed later). D_2 carries dimensions of area, and the ratio D_2/τ is a diffusion coefficient for voltage change: In a time t, a voltage perturbation is expected to propagate on a two-dimensional sheet through an rms distance $\sqrt{4D_2t/\tau}$.

The terms comprising D_2 make intuitive sense. Diffusion strength will increase with a, the areal extent of dendritic sensitivity, and will increase with gap-junction connectivity, N_{ii}^{γ}. While decreases in gap-junction resistance R_g (i.e., increases in gap conductance) will increase coupling, decreases in membrane resistance R_m will *weaken* coupling, since the diffusive currents will tend to be shunted to ground. Conversely, increases in membrane resistance will tend to increase the isolation of the soma voltage, allowing diffusive effects to persist longer.

For simplicity, this derivation for diffusive coupling strength D_2 has assumed an idealized square "top-hat" profile for the zone of dendritic sensitivity. In the Appendixes we investigate two alternative connectivity schemes: A two-dimensional Gaussian distribution function centered on the neuron of interest (Appendix A), and an area-overlap distribution which assumes that the probability that a pair of neurons is gap-junction connected is proportional to the area of overlap of two equal-area uniformly-weighted circular disks (Appendix B). Although the latter distributions give weaker estimates for the D_2 coupling strength (see below for further discussion), all three derivations predict a consistent scaling relationship of the general form $D_2 \sim uN^{\gamma}R_m/R_g$, where u is "effective area" of the Fukuda diffusion cell.

4. Estimation of diffusive coupling strengths

Using electron micrographic length measurements, Fukuda *et al.* estimated that the single-junction conductance for L-type interneurons lies in the range 2.0–5.0 nS. This is a theoretical maximum value that assumes that all of the connexin proteins are in their open conformation, and is broadly consistent with the measured inhibitory gap-junction conductances reported by Galarreta and Hestrin [21], and by Gibson *et al.* [22]. Taking the middle of this range leads to a gap resistance estimate of $R_g = 290\ \mathrm{M}\Omega$.

Fukuda and colleagues did not report the average membrane resistance for L-type interneurons, so we will make an estimate for R_m based on neuron size, specific capacitance c_m (capacitance per unit area) for neuronal membrane, and our mean-field model value for inhibitory time-constant $\tau_i = 40$ ms (see Table I). Assuming the L-type neurons are spherical with average cross section $\pi r^2 = 200\ \mu\mathrm{m}^2$ (we infer this value from Fukuda's Fig. 3A size-distribution histogram), the surface area will be $A = 4\pi r^2 = 800\ \mu\mathrm{m}^2$. The "traditional" value for c_m is 1.0 $\mu\mathrm{F/cm}^2$, but Koch ([38], p. 482) suggests that this is probably an overestimate, since the capacitance of a pure bilayer lipid membrane without proteins

TABLE II. Effective diffusion-cell area, u, and corresponding diffusive coupling strength for three models for gap-junction connectivity. The Gaussian variance estimate $\sigma^2 \approx 0.026$ mm^2 was obtained by applying a Gaussian fit to Fig. 5B (top panel) of Fukuda *et al.* [26]. The diffusion strengths are computed using $D_2 = uN^\gamma R_m/4R_g$ for $u \in \{a, b^2, \sigma^2\}$, with $N^\gamma = 60$, $R_m = 7100$ MΩ, $R_g = 290$ MΩ.

Connectivity	Effective cell area, u (mm^2)	Diffusive strength (cm^2)
Top-hat	$a = 0.16$	$D_2 = 0.6$
Heaviside disk	$b^2 = 0.04$	$D_2^{\mathrm{H}} = 0.15$
Gaussian	$\sigma^2 = 0.026$	$D_2^{\mathrm{G}} = 0.1$

is between 0.6 and 0.8 μF/cm^2. Taking the middle of this range, the capacitance will be $C = c_m A = 5.6$ pF, and the membrane resistance will be $R_m = \tau_i / C = 7.1$ GΩ. We highlight the observation by Koch *ibid.* that measured values for R_m vary widely with the quality of the intracellular recording and with the amount of synaptic input into the cell; as recording techniques become more mature and sophisticated, the estimates of R_m tend to increase.

We can now make a rough estimate for D_2, the diffusive coupling strength for L-type inhibitory neurons. Substituting $a = 0.0016$ cm^2, $N_{ii}^\gamma = 60$, $R_m = 7100$ MΩ, and $R_g = 290$ MΩ, gives $D_2 = aN_{ii}^\gamma R_m/4R_g = 0.6$ cm^2. This is an intriguing result, since, as we will discuss below in Sec. III A (and as demonstrated in Fig. 4), this is very close to the critical value for inhibitory diffusion that will destabilize a spatially homogeneous model cortex, leading to the formation of Turing structures. Larger values of D_2 are sure to form spatial patterns; smaller values are too weak to promote self-organization.

Note that our $D_2 \approx 0.6$ cm^2 value for diffusive strength is based on the idealized assumptions that (i) *all* L-type inhibitory neurons falling within the Fukuda zone of diffusive sensitivity of a given neuron will be gap-junction connected to that neuron (and vice versa); and that (ii) all connexin-36 channels within each gap junction are in their fully-open configuration. When the "top-hat" idealization (i) is replaced by a Gaussian model for connectivity (Appendix A), or by an area-overlap model for pairs of Heaviside-weighted disks (Appendix B), we obtain D_2 estimates that are smaller than the top-hat value by factors of ~6 and 4, respectively—see Table II—suggesting that $D_2 \approx 0.6$ cm^2 is probably an overestimate of the true value. Despite this, we have elected to retain the top-hat estimate for the following reasons.

(1) Detection and identification of gap junctions is a technically challenging undertaking; consequently, quoted values for gap-junction abundance in the cerebral cortex have been increasing—and are likely to continue increasing—over time as clinical and laboratory techniques become more sensitive and discriminating. For example, it has only recently been discovered that, in addition to the *connexin* family of proteins, there exists a distinct alternative family of gap-junction forming proteins—the *pannexins* [39]. Pannexins are found abundantly in both excitatory and inhibitory neurons throughout the cortex, and have been detected in cortical areas hitherto thought to have been devoid of gap junctions [40]. Thus gap-junction connectivity appears to be a structural feature that is ubiquitous throughout the cerebral cortex.

(2) Only interneuron-to-interneuron connectivity via connexin-36 (Cx36) gap junctions has been quantified by Fukuda *et al.* [26]. An earlier paper by Nadarajah *et al.* [41] found copious gap-junction connections between neurons and their supporting *glial* cells via Cx32 connexin, and between pairs of glial cells via Cx43. Alvarez-Maubecin *et al.* [42] have demonstrated functional coupling between neurons and adjacent glia (astrocytes), mediated by gap junction connections. It seems plausible that the glial scaffolding that underpins the entire neuronal network will tend to strengthen diffusive coupling between neurons by way of neuron-glial-neuron circuits.

(3) The Fukuda *et al.* measurements are specific to Cx36 gap junctions, and are not sensitive to other connexins. The Nadarajah *et al.* [41] paper shows that gap junctions based on Cx32 and Cx43 are abundant in all layers of the cerebral cortex of the adult rat, so would be expected to be abundant in other mammalian brains (such as cat and human) also. Using immunocytochemical staining techniques in the rat frontal cortex, Nadarajah detected 4000 Cx32 puncta (cell perforation) markers per mm^2, and 20 000 Cx43 puncta per mm^2; the corresponding Cx36 density (in cat visual cortex) reported by Fukuda is 24 000 mm^{-2} (400 L-type interneurons per mm^2, with 60 gap junctions per neuron).

Idealization (ii) assumes that all Cx36 channels are fully open, consistent with the low-resistance pathways that have been measured for the immature cortex during corticogenesis and neuronal circuit formation [41]. However, in their discussion, Fukuda *et al.* [26] note that in a mature (rat) cortex there is evidence that only 2% to 5% of the channels are simultaneously open, leading to an estimate for gap-junction conductance that will be lowered by a factor of about 25. It is plausible that the additional sources of gap-junction connectivity listed above (undetected connexin types, glial-cell diffusive scaffolding) might be sufficient to compensate for partially open channels.

In contrast to the case for inhibitory neurons, there are very few reports for gap-junction connectivity between *excitatory* neurons [43], and none suggesting the existence of a dense network of e-to-e resistive connections. Indeed, such e-to-e coupling, where it has been detected, seems to be both rare and sparse; this finding is consistent with a recent theoretical analysis by Ermentrout [44] showing that strong gap-junction coupling between excitatory cells leads to the death of network activity. Accordingly, we will set the excitatory diffusion coefficient to be a small, but nonzero, fraction of the inhibitory value:

$$D_1 = D_2/100. \tag{12}$$

Although we take this to be our default setting, in some of our numerical simulations we will allow the excitatory diffusion coefficient to approach the inhibitory value in order to explore the theoretical consequences of diffusivities that are closer to being in balance.

We now present the standard mean-field cortical model, augmented with gap-junction diffusion terms. We then investigate, theoretically and in grid simulations, the properties of

the augmented model in the strong-diffusion limit, choosing values of the D_2 inhibitory coupling strength that are considerably *larger* than that we have deduced from Fukuda's measurements. We will show that interesting new behaviors emerge when a strong inhibitory diffusion permeates the entire cerebral cortex, and we suggest that these altered behaviors may be of significant neurobiological interest.

B. Model equations

The derivation of Eq. (10) focused on the effect of diffusive gap current, $I_{\rm gap}$, entering the soma. We now need to include the contribution from synaptic current, $I_{\rm syn}$, entering due to spike activity at *chemical* synapses. The voltage perturbations arising from synaptic input are described by the standard (diffusionless) mean-field cortical model detailed in our earlier papers [11,13]; adding the diffusive perturbation terms gives the following revised equations,

$$\tau_e \frac{\partial V_e}{dt} = V_e^{\rm rest} - V_e + [\rho_e \psi_{ee} \Phi_{ee} + \rho_i \psi_{ie} \Phi_{ie}] + D_1 \nabla^2 V_e, \tag{13}$$

$$\tau_i \frac{\partial V_i}{dt} = V_i^{\rm rest} - V_i + [\rho_e \psi_{ei} \Phi_{ei} + \rho_i \psi_{ii} \Phi_{ii}] + D_2 \nabla^2 V_i, \tag{14}$$

where the terms in square brackets $[\cdots]$ are the synaptic contributions to the time-course of the excitatory and inhibitory soma voltages. Here, ρ_e and ρ_i are the synaptic coupling strengths of the *chemical* synapses given by the area under the excitatory and inhibitory postsynaptic potential (PSP) impulse-response functions; note that these are *signed* quantities with $\rho_e > 0$ (excitation), and $\rho_i < 0$ (inhibition), and carry units mV s. The factors ψ_{ee}, ψ_{ie}, ψ_{ei}, and ψ_{ii} appearing in Eqs. (13) and (14) are normalized reversal-potential functions [5,45],

$$\psi_{ek} = \frac{V_e^{\rm rev} - V_k}{V_e^{\rm rev} - V_k^{\rm rest}}, \quad k = e,i, \tag{15}$$

$$\psi_{ik} = \frac{V_i^{\rm rev} - V_k}{V_i^{\rm rev} - V_k^{\rm rest}}, \quad k = e,i, \tag{16}$$

where $V_{e,i}^{\rm rev}$ is the synaptic reversal voltage for neurons of type e,i, and $V_k^{\rm rest}$ is their resting voltage. Φ_{ee} and Φ_{ie} are the excitatory and inhibitory flux inputs (units: spikes/s) entering the excitatory population. These obey second-order differential equations,

$$\left(\frac{d}{dt} + \gamma_{ee}\right)^2 \Phi_{ee} = \gamma_{ee}^2 [N_{ee}^{\alpha} \phi_{ee} + N_{ee}^{\beta} Q_e + \phi_{ee}^{\rm sc}], \tag{17}$$

$$\left(\frac{d}{dt} + \gamma_{ie}\right)^2 \Phi_{ie} = \gamma_{ie}^2 N_{ie}^{\beta} Q_i, \tag{18}$$

and the corresponding flux inputs Φ_{ei} and Φ_{ii} reaching the inhibitory population are

$$\left(\frac{d}{dt} + \gamma_{ii}\right)^2 \Phi_{ii} = \gamma_{ii}^2 N_{ii}^{\beta} Q_i, \tag{19}$$

$$\left(\frac{d}{dt} + \gamma_{ei}\right)^2 \Phi_{ei} = \gamma_{ei}^2 [N_{ei}^{\alpha} \phi_{ei} + N_{ei}^{\beta} Q_e + \phi_{ei}^{\rm sc}]. \tag{20}$$

Note that the double-subscripting is to be read left-to-right, thus Φ_{ei} is shorthand for $\Phi_{e\to i}$, meaning flux originating *from* the population-average excitatory neuron *to* the population-average inhibitory neuron.

Following Robinson *et al.* [4], the long-range excitatory fluxes ϕ_{ek} in Eqs. (17) and (20) are modelled as damped waves generated by sources Q_e obeying the 2D wave equations,

$$\left[\left(\frac{\partial}{\partial t} + v\Lambda_{ek}\right)^2 - v^2\nabla^2\right]\phi_{ek} = v^2 \Lambda_{ek}^2 Q_e, \quad k = e,i, \tag{21}$$

where v is the average axonal conduction speed and Λ_{ek} is an inverse-length scale for the long-range connections.

Q_e and Q_i are sigmoidal functions that map membrane voltage $V_{e,i}$ to population-averaged firing rates [5],

$$Q_k = \frac{Q_k^{\max}}{1 + \exp[-C(V_k - \theta_k)/\sigma_k]}, \quad k = e,i, \tag{22}$$

where $C = \pi/\sqrt{3}$, θ_k is the population-average threshold voltage for firing, σ_k is its standard deviation, and $Q_k^{\max}$ is the maximum firing rate for the $k = e,i$ neural population.

Equations (13)–(21) define a set of eight coupled stochastic differential equations for the 2D cortex. The stochasticity, entering via subcortical sources $\phi_{ee}^{\rm sc}$ and $\phi_{ei}^{\rm sc}$ in Eqs. (17) and (20), is modeled as Gaussian-distributed white-noise perturbations superimposed on a mean level of incoming subcortical activity $\langle \phi_{ek}^{\rm sc} \rangle$:

$$\phi_{ek}^{\rm sc} = s\langle \phi_{ek}^{\rm sc} \rangle + \sqrt{s\langle \phi_{ek}^{\rm sc} \rangle} \cdot \xi_m(\vec{r},t), \quad m = 1,2,\ k = e,i. \tag{23}$$

Here, s is a dimensionless scale factor that allows us to vary the level of subcortical driving. The two $\xi_m(\vec{r},t)$ stochastic terms are independent, zero-mean, white-noise sources that are delta-correlated in time and space:

$$\langle \xi_m(\vec{r},t) \rangle = 0, \tag{24}$$

$$\langle \xi_m(\vec{r},t)\xi_n(\vec{r}',t') \rangle = \delta_{mn}\delta(t-t')\delta(\vec{r}-\vec{r}'). \tag{25}$$

C. Effect of gap junctions

Drawing on previous experience with anesthesia and sleep versions of this model [6–8,10–13] and from a theoretical study of a near-threshold single neuron model [46], we anticipate that the richest, most interesting dynamics are likely to occur when the cortical system is close to a "decision point." By this we mean that the cortex is free to make a choice between two (or more) equilibrium states [6,7,11,13], or between an equilibrium state and a dynamic state (such as a limit cycle) [8,10,12]. In these cortical studies, we controlled one or two selected neurotransmitter parameters to drive the cortex through its anesthesia and sleep-cycling state changes; for the present work, we choose to follow Wright [15,47], and use subcortical input flux $\phi^{\rm sc}$ en-

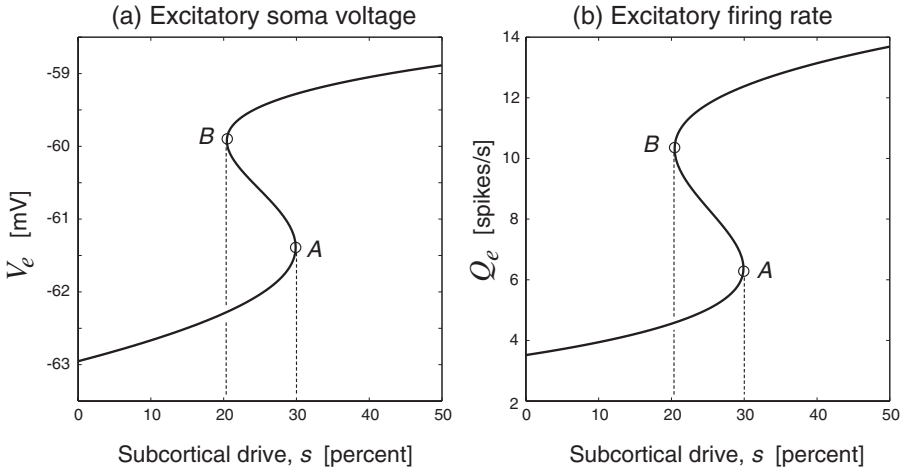

FIG. 3. Distribution of steady states for the noiseless homogeneous cortical model as a function of subcortical drive. Panel (a) shows the locus of equilibrium membrane voltages V_e for the excitatory neural population; (b) shows the corresponding excitatory firing rates Q_e. Graphs (a) and (b) are linked via the sigmoidal mapping of Eq. (22). Turning points A and B demarcate the region of multiple steady states, $0.2 \lesssim s \lesssim 0.3$, for which the population can either reside in the low-firing *quiescent* state (bottom branch), or in the high-firing *activated* state (top branch). The AB midbranch is unstable with respect to small perturbations.

tering Eqs. (17) and (20) as the control parameter that enables us to explore the distribution of equilibrium states available to the *noiseless homogeneous* cortex. We will then allow subcortical noise to enter, and investigate how the introduction of gap-junction diffusion leads to the spontaneous creation of far-from-equilibrium spatially inhomogeneous Turing states.

1. Equilibrium manifold

To locate the manifold of homogeneous steady states, we zero the ξ_m fluctuating term in Eq. (23), and allow the subcortical drive s to vary from zero (no subcortical input) to unity (maximum subcortical input),

$$\phi^{\mathrm{sc}}_{ee,ei} = s\langle \phi^{\mathrm{sc}}_{ee,ei} \rangle, \quad 0 \leq s \leq 1. \tag{26}$$

For each value of s, we set $d/dt = \nabla^2 = 0$ in differential equations (13)–(21) to remove all time and space dependence, and solve numerically the resulting set of coupled nonlinear algebraic equations for the homogeneous steady-state values of the 10 system variables V_e^{o}, V_i^{o}, Q_e^{o}, Q_i^{o}, ϕ_{ee}^{o}, ϕ_{ei}^{o}, Φ_{ee}^{o}, Φ_{ei}^{o}, Φ_{ie}^{o}, Φ_{ii}^{o}, with parameter values as listed in Table I.

Figure 3 shows graphs of the distribution of V_e^{o} and Q_e^{o} equilibrium values as a function of subcortical drive. We observe that there is a multistate region for subcortical activity in the range $0.2 \lesssim s \lesssim 0.3$. In this subspace, the cortex has three equilibrium states available to it (we elucidate their relative stabilities shortly). We emphasize that the steady-state manifolds of Fig. 3 are *completely independent* of the D_1 and D_2 diffusion coefficients, since their Laplacian operators ∇^2 have been explicitly zeroed here. However, as we demonstrate below, these diffusion terms can *destabilize* the equilibrium manifold, leading to an inhomogeneous pattern of nonequilibrium steady states distributed over the entire 2D sheet of cortical tissue.

2. Stability analysis

We performed a stability analysis of the deterministic (i.e., noiseless) parts of Eqs. (13)–(21), linearizing about the homogeneous equilibrium manifold illustrated in Fig. 3. The analysis is simplified by taking advantage of the parameter-value symmetries evident in Table I: $V_e^{\mathrm{rest}} = V_i^{\mathrm{rest}}$; $\tau_e = \tau_i$; $\gamma_{ee} = \gamma_{ei}$; $\gamma_{ie} = \gamma_{ii}$; $N_{ee}^{\alpha} = N_{ei}^{\alpha}$; $N_{ee}^{\beta} = N_{ei}^{\beta}$; $N_{ie}^{\beta} = N_{ii}^{\beta}$; $\Lambda_{ee} = \Lambda_{ei}$. With these parameter symmetries, ϕ_{ee} and ϕ_{ei} obey the same equation of motion, as do the pairs (Φ_{ee}, Φ_{ei}) and (Φ_{ie}, Φ_{ii}); but note that the symmetry between the V_e and V_i equations—for homogeneous cortex—will be broken by the presence of unequal D_1 and D_2 diffusion coefficients. The physiological evidence (reviewed above in Sec. II A 4) suggests that, in cortical tissue, inhibitory diffusion strongly dominates excitatory diffusion, $D_2 \gg D_1$.

With these simplifications, our cortical system reduces to five coupled differential equations (DEs): Two first-order (V_e, V_i), and three second-order $(\Phi_{ek}, \Phi_{ik}, \phi_{ek})$. Reformulating the second-order equations as pairs of first-order DEs results in a set of eight coupled first-order DEs. We linearize these eight DEs by assuming that each variable can be expressed as its homogeneous equilibrium value plus a fluctuating component. For example, we write the excitatory soma voltage as

$$V_e(\vec{r},t) = V_e^{\mathrm{o}} + \delta V_e(\vec{r},t), \tag{27}$$

where $\vec{r}$ is the 2D position vector and δV_e is the fluctuation about the equilibrium value V_e^{o}. We link the fluctuation δV_e to its spatial Fourier transform $\widehat{\delta V_e}$,

$$\delta V_e(\vec{r},t) = \frac{1}{(2\pi)^2} \int_{-\infty}^{\infty} \widehat{\delta V_e}(\vec{q},t) e^{i\,\vec{q}\cdot\vec{r}} d\vec{q}, \tag{28}$$

where $\vec{q}$ is the 2D wave number vector. After linearizing, then Fourier transforming the eight DEs—with each occurrence of ∇^2 replaced by $-q^2$ (where $q = |\vec{q}|$)—we compute

numerically the eigenvalues of the 8×8 Jacobian matrix evaluated at homogeneous equilibrium for a finely spaced range of wave numbers, q. Three of the 64 Jacobian-matrix elements are q-dependent (two diffusion Laplacians plus a wave-equation Laplacian), so, in general, the eigenvalue structure, and therefore overall system stability, is a function of wavenumber. The stability is determined by the real part of the largest (most positive, or least negative) eigenvalue of the Jacobian matrix: If the dominant eigenvalue has a positive real part, the perturbation will grow, and the equilibrium is unstable; if the dominant eigenvalue has a negative real part, the perturbation will decay, indicating a stable equilibrium.

III. RESULTS

A. Dispersion relations and stability

Figure 4 shows a representative sample of dispersion curves for subcortical drive-fraction $s=0.25$, plotted as a function of scaled wave number $q/2\pi$. We select three settings of gap-junction diffusion (in cm^2): $(D_1,D_2)=(0,0)$ (no diffusion, dash-dot curve); (0.006,0.6) (weak diffusion, solid curve); (0.03,3.0) (strong diffusion, dashed curve). Because the homogeneous cortex has access to *three* steady states at this value of s (see Fig. 3 and its three miniature insets in Fig. 4), we plot three sets of curves for each of (a) top branch; (b) midbranch; (c) bottom branch. The vertical axis is the real part of the *leading* eigenvalue—the nondominant eigenvalues have more negative real parts, therefore make a negligible contribution to cortical stability and are not plotted here. With the default Table I values, the leading eigenvalue Λ can become complex, $\Lambda=\alpha\pm i\omega$ [e.g., for $q/2\pi \gtrsim 0.3$ for the $D_2=0$ curve of panel (a)], but these oscillatory modes are heavily damped (i.e., real part α is strongly negative), so oscillatory instabilities (i.e., standing waves: $\alpha>0$, $\omega\neq 0$ at $q=0$; or traveling waves: $\alpha>0$, $\omega\neq 0$ for nonzero q) are *not* predicted. To simplify the graphs, we have suppressed the plotting of the imaginary eigenvalue parts.

The strong-, weak-, and zero-diffusion curves all converge at $q=0$, the homogeneous, "infinite-wavelength" limit. Close inspection at this left-edge extreme shows that the top- [panel (a)] and bottom [panel (c)] branch equilibria are stable (have negative dominant eigenvalue) at $q=0$, while the mid-branch [panel (b)] is unstable. (We note that, with some parameter adjustments, the top and bottom branches can destabilize via Hopf bifurcations [10], but we do not pursue those instabilities here.)

For the case of zero diffusion ($D_2=0$, dash-dot curve), increasing the spatial wave number predicts *greater* stability (more negative eigenvalue) for the top-branch (a) and bottom-branch (c) homogeneous steady states. In contrast, the weak-diffusion case ($D_2=0.6$ cm^2, solid curve) predicts a bottom-branch instability will develop at $q/2\pi\approx 0.27$ cm^{-1}, corresponding to a wavelength of $\lambda\approx 3.7$ cm. Further increases in the inhibitory diffusion increase the range of spatial frequencies that can destabilize the homogeneous equilibrium. For example, with $D_2=3.0$ cm^2 (dashed curve), instabilities can develop for $0.05\lesssim q/2\pi\lesssim 0.6$ cm^{-1}, with maximum growth predicted at $q/2\pi\approx 0.285$ (top branch) and $q/2\pi\approx 0.26$ cm^{-1} (bottom branch). The average of these two linearized predictions gives a useful estimate of the effective spatial frequency of the fully-developed Turing labyrinth [see Fig. 8 and panel (1) of Fig. 6].

Figure 4 curves describe cortical stability for subcortical drive fraction $s=0.25$, a setting for which multiple steady states exist. We have also explored the stability at positions far from the multiple-steady-state region (e.g., $s=0.05$ and $s=0.50$; not shown here), and find that, provided the D_2 coupling strength is sufficiently large, Turing instabilities are predicted here also. These predictions have been verified in simulation runs. We conclude that multiple steady states are *not essential* for Turing formation. However, we have observed that as the operating point is moved away from the multiroot region, larger values of D_2 are required to trigger a Turing instability, and, conversely, that the multiroot region $0.20\lesssim s\lesssim 0.30$ provides a "sweet spot" within which rather smaller values of diffusive coupling are sufficient to precipitate Turing patterns. Thus, while $D_2=0.6$ cm^2 is *just sufficient* to trigger pattern formation within the sweet zone at $s=0.25$, this coupling strength is too weak to trigger patterns when $s<0.20$ or $s>0.30$.

B. Grid simulations

The linearized theory predicts that the homogeneous steady state of the cortex will become destabilized by the presence of gap-junction diffusive currents flowing between populations of inhibitory neurons. To test these predictions, we ran an extensive series of two-dimensional grid simulations of the full, nonlinear cortical equations (13)–(21). Our model cortex was a square sheet with periodic (toroidal) boundary conditions, of side 25 cm, with grid spacing $\Delta x=\Delta y=1$ mm, corresponding to a rectangular grid containing $250^2=62\,500$ sample points. We used an Euler integration with time-step $\Delta t=0.01$ ms. For all of the runs presented here, the firing rates and soma voltages were initialized to the $s=0.25$ mid-branch steady-state values. All grid points were then perturbed continuously by random subcortical input (unfiltered spatio-temporal white noise), and the subsequent evolution of the cortical sheet was traced for a total time of 4000 ms (i.e., 400 000 time steps). The diffusion and wave equation Laplacians were implemented as a circular convolution of the 3×3 second-difference operator $\mathbf{L}$,

$$\mathbf{L}\equiv\begin{bmatrix}0 & 1 & 0\\ 1 & -4 & 1\\ 0 & 1 & 0\end{bmatrix},$$

acting on the relevant grid variable using the `convolve2()` function [48]. Computer codes were written in MATLAB 5.2 (1.42-GHz PowerPC laptop) for reduced-resolution test runs, then ported to MATLAB 7.1 (Linux server with 3-GHz Xeon processor) for final production runs. Each full-resolution 4-s run required ~20 h of Xeon processor time.

Figure 5 shows snapshots of the evolution of a Turing pattern at ~1-s intervals for strong inhibitory diffusion, $D_2=3$ cm^2, with moderately strong excitatory diffusion, $D_1=D_2/4=0.75$ cm^2. The top row of images are bird's-eye im-

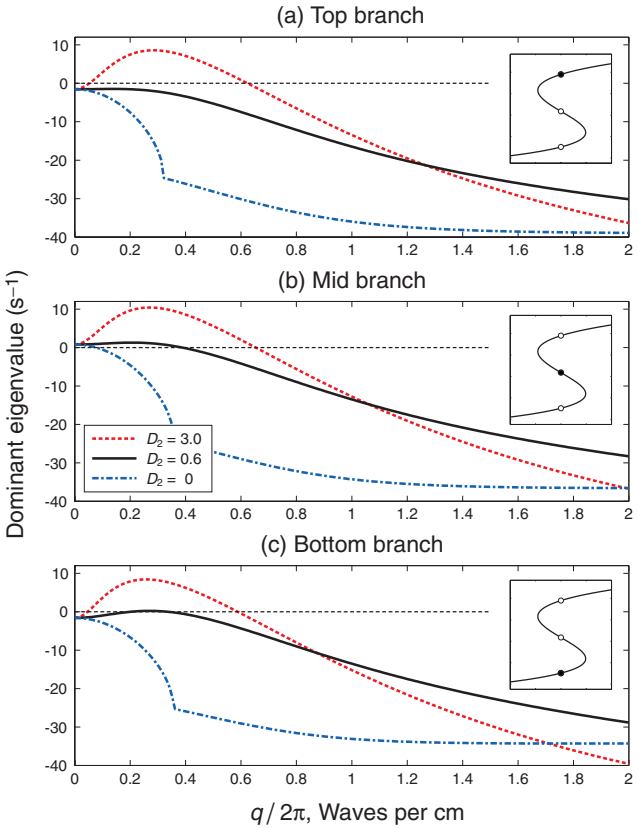

FIG. 4. (Color) Dispersion curves for the gap-junction mediated cortical model defined by Eqs. (13)–(21). The real part of the dominant eigenvalue is plotted as a function of (scaled) wave number, $q/2\pi$, for three values of D_2, the inhibitory diffusion coefficient (with units cm^2): 3.0 (dashed red curve); 0.6 (solid black curve); 0 (dash-dotted blue curve). The excitatory diffusion coefficient is set at $D_1=D_2/100$. The three separate graphs correspond to the (a) top-, (b) middle-, and (c) bottom-branch equilibrium states at subcortical drive $s=0.25$ [inset S bends are miniatures of Fig. 3(b)]. The homogeneous state is predicted to be unstable at all spatial frequencies for which the dispersion curve is positive. Note the general trend: Stronger diffusion leads to greater instability.

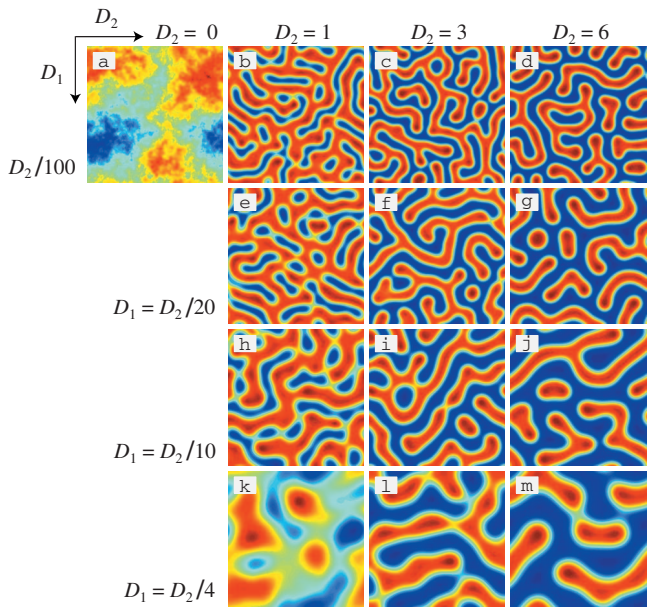

FIG. 6. (Color) Gallery of diffusion-induced Turing patterns in a square cortex of side 25 cm with periodic boundaries. The gallery is arranged with inhibitory diffusion, D_2, increasing *to the right*, and excitatory diffusion, D_1, expressed as a fraction of D_2, increasing *down* the page. Each panel shows a snapshot of the noise-driven cortex after 4 s of evolution from the unstable midbranch at $s=0.25$ (see Fig. 5 for details). Panel (a) shows the case of zero diffusion: The cortex organizes into a diffuse, cloudlike pattern (final maximum and minimum firing rates were 8.7 and 8.4 s^{-1}), but does not crystalize into a Turing structure. All other cases [panels (b)–(m)] evolve into stable serpentine Turing patterns containing alternating regions of low- (blue) and high-firing (red) states. (Grid resolution is 1 mm; time step is 0.01 ms.)

age plots of the excitatory-to-excitatory firing-rate flux ϕ_{ee} [from wave equation (21)], and the bottom row is the same information viewed on a 3D mesh. The cortex is initialized at the unstable midbranch corresponding to subcortical drive $s=0.25$, and stimulated with low-intensity white noise, giving the $t=0$ left-hand images their speckled appearance. By

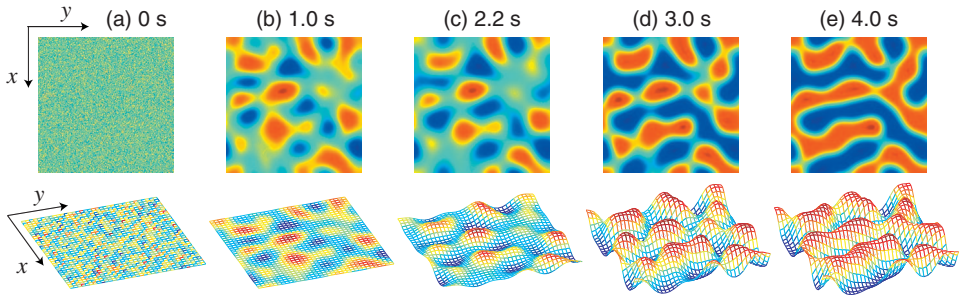

FIG. 5. (Color) Spontaneous development of a stationary Turing pattern in excitatory firing-rate flux, ϕ_{ee}, starting from a homogeneous equilibrium state perturbed by spatiotemporal white noise. This sequence shows the 4-s evolution of the model cortex with diffusion coefficients $D_2=3.0$ cm^2 and $D_1=0.75$ cm^2 [see panel (l) of Fig. 6]. The cortex is modeled as a square grid of side 25 cm with periodic (toroidal) boundaries. The initial state is the unstable midbranch equilibrium point at $s=0.25$ [see Fig. 3 and the inset of Fig. 4(b)]. Grid resolution is $\Delta x=\Delta y=1$ mm, giving a grid size of 250×250 sample points; this grid is subsampled to produce the second-row mesh images; time step is 0.01 ms. Other parameter settings as displayed in Table I. At time $t=4$ s, the maximum (displayed as red) and minimum (blue) firing rates are 16.8 and 2.8 s^{-1}, respectively—see Fig. 7 for time series plots.

time $t=1$ s, the cortex has organized itself into localized islands and troughs of firing-rate activity. For $t \gtrsim 2$ s, we see the contrast between higher- and lower-firing regions increasing, with the islands merging to form rolling "mountain ranges" of high activity, surrounded by valleys of low firing activity. The fully developed image is presented in panel (l) of Fig. 6, and the time-development of selected points within the grid is plotted in Fig. 7(d).

Figure 6 presents a gallery of gap-junction-mediated Turing structures for a range of inhibitory (D_2) and excitatory (D_1) diffusion-coefficient combinations. The top-left image (a) has no diffusion, so the homogeneous equilibrium state fails to precipitate into a Turing pattern. Nevertheless, the cloudlike appearance indicates a very slow spatial fluctuation whose long-range ordering heralds an imminent phase change: if the simulation were run for a longer time (or if the noise amplitude were increased), the entire cortex would "fall" off the unstable equilibrium into either the high-firing or the low-firing homogeneous equilibrium state, whereupon all spatial structure would dissipate.

Panels (b)–(m) of Fig. 6 illustrate the range of striking Turing structures that can "crystalize" from the homogeneous state when gap-junction diffusion is enabled—provided that inhibitory diffusion is dominant (i.e., $D_2 > D_1$). Scanning the images from left to right, we observe that successive increases in D_2 inhibitory diffusion tend to *enhance* the firing-rate contrast between high- and low-activity regions, while simultaneously increasing the separation between activated regions. Conversely, scanning from top to bottom, we note that increases in D_1 excitatory diffusion *reduce* the firing-rate contrast, broaden the spatial extent of the activated regions, and slow the rate of Turing precipitation. These D_1-induced reductions in contrast, coupled with slowed evolution, are illustrated clearly in Fig. 7 where we see the detailed time development at 10 selected grid points in the four panels labeled (c), (f), (i), (l) in the Fig. 6 image gallery.

To confirm the spatial-periodicity prediction of the linearized dispersion relations plotted in Fig. 4, we computed the two-dimensional Fourier amplitude spectrum for the Fig. 6(c) Turing pattern generated with $(D_1, D_2) = (0.03, 3.0)$ cm^2. The result, shown in Fig. 8(a), hints at a circular spectral distribution, indicative of a fixed spatial frequency whose wave vector has no preferred direction. This is clarified by growing 16 independent Turing patterns—each realized with distinct subcortical white-noise sequences but otherwise identical parameter values—computing the Fourier spectrum for each pattern, then averaging the 16 spectra. This averaging procedure improves the signal-to-noise ratio by about a factor of 4: See Fig. 8(b). The patchy circle in (a) has become a bright annulus of radius ~ 0.28 cm^{-1}, in pleasing agreement with the predicted wavenumber for maximum instability indicated in Fig. 4 (dashed curve).

IV. DISCUSSION

A. Cortex as a reaction-diffusion reactor

With the inclusion of diffusion effects into a continuum description of the cortex, we have transformed to a model that is mathematically equivalent to a *reaction–diffusion* system containing a pair of competing *activator* and *inhibitor* morphogens—chemical species that diffuse and react to generate spatial structure and patterns [27]. The inhibitor suppresses production of both itself and the other chemical; the activator promotes the production of both morphogens. In the cortex, active inhibitory neurons release neurotransmitters (e.g., GABA) that suppress the firing of both inhibitory and excitatory neurons, while excitatory neurons release neurochemicals (e.g., AMPA) that tend to excite the firing activity of both neuron populations. This suggests the following mean-field equivalences:

Chemical system	Cortical system
[*inhibitor* concentration]	≡ [firing rate of *inhibitory* neural population]
[*activator* concentration]	≡ [firing rate of *excitatory* neural population]

It is well established that a necessary condition for the formation of spatial patterns in a chemical reactor is that the inhibiting substance must diffuse *more rapidly* than the activator [28,29]. Suppose that an initial homogeneous equilibrium state is perturbed by a small localized increase in activator concentration. This disturbance will increase the local production of both species. But the inhibitor, being more mobile, will diffuse away more rapidly, lowering activity in the surrounding region while simultaneously allowing a further increase in local activity. Thus the homogeneous symmetry is broken by the accelerating development of local curvature in concentration gradients, with these changes propagating outwards to create concentration peaks and troughs throughout the reactor.

Carrying these ideas to the cortical model, we see that the inclusion of gap-junction diffusion fulfills the required condition for spontaneous spatial patterning of neural activity in a natural and graceful manner. The presence of bountiful gap-junction connections between inhibitory neurons [21–23,26], and the paucity of gap-junction connections between excitatory neurons [43] means that inhibitory diffusivity, D_2, is likely to be considerably stronger than excitatory diffusivity, D_1. As predicted by linear stability analysis of our two-dimensional mean-field cortical model (see Sec. III A

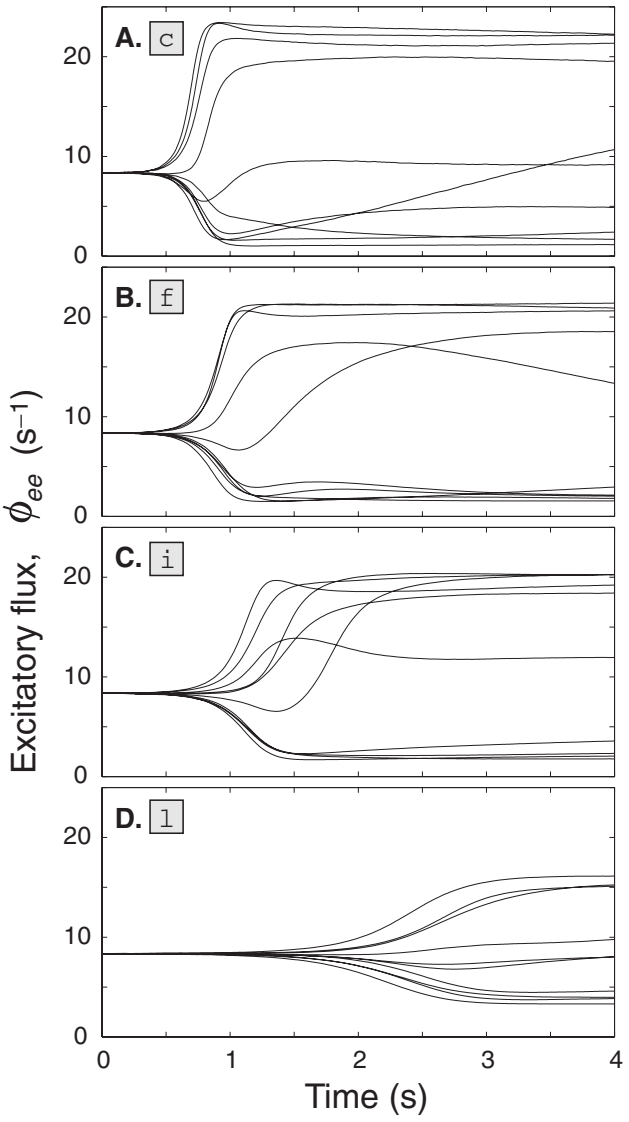

FIG. 7. Four-second time development of excitatory flux ϕ_{ee} at 10 representative grid points for the Turing patterns shown in panels (c), (f), (i), and (l) of Fig. 6. The 10 sample points are located at regular 2.5-cm intervals down the midpoint vertical at $y=12.5$ cm. [Grid snapshots for the time evolution of panel (l) are displayed in Fig. 5.] In each case, the grid was initialized at the unstable mid-branch equilibrium point at subcortical drive $s=0.25$, for which the excitatory firing rate is $\phi_{ee}^{o}\approx 8.35$ s^{-1}, and driven continuously with spatiotemporal white noise. For this set of panels, inhibitory diffusion is held constant at $D_2=3.0$ cm^2, and excitatory diffusion D_1 (in cm^2) increases down the panels: (**a**) $D_1=0.03$; (**b**) $D_1=0.15$; (**c**) $D_1=0.30$; (**d**) $D_1=0.75$. Increased excitatory diffusion produces a slowed Turing growth, with diminished contrast between the final high- and low-firing states.

and Fig. 4), and subsequently verified by nonlinear stochastic grid simulations (Sec. III B and Figs. 5–7), the homogeneous steady state is destabilized in the presence of dominant inhibitory diffusion, and evolves promptly into labyrinthine Turing patterns consisting of alternating patches of activated and inactivated cortical tissue. The size, shape, connectedness, and rate of evolution of the activated labyrinths depends on both the absolute magnitude of D_2, and on the D_2/D_1 ratio, with the largest "island" structures in Fig. 6 occurring when $D_2/D_1\approx 4$.

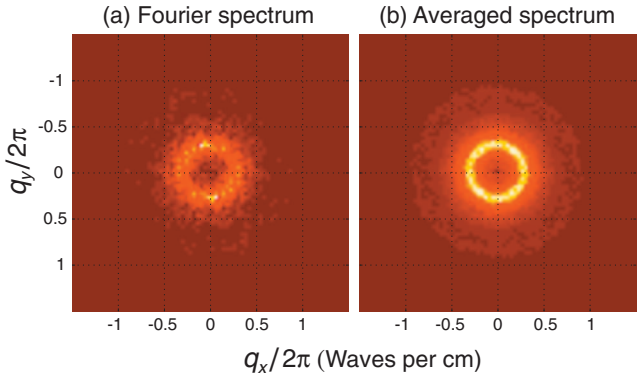

FIG. 8. (Color) Fourier amplitude spectrum of the Turing pattern of Fig. 6, panel (c): $(D_1,D_2)=(0.03,3.0)$ cm^2. (a) Single-pattern spectrum. (b) Average of 16 spectra from 16 different panel (c) patterns (not shown), each pattern generated using a different white-noise sequence. The bright annular ring in (b) has average radius $q/2\pi\approx 0.28$ cm^{-1}, consistent with the peak in the $D_2=3.0$ dispersion-curve predictions of Fig. 4.

B. Gap-junction modeling assumptions

We have shown theoretically that the formation of large-scale patterns of cortical activity depends crucially on the strength of the gap-junction diffusion that couples the population of inhibitory neurons. Our incorporation of diffusive coupling within an existing mean-field synaptic model of electrocortical activity is based on the microanatomical measurements of Fukada *et al.* [26]. The resulting "diffusion-enhanced" model inherits all of the simplifying assumptions embedded the original mean-field synaptic cortex:

(1) All inhibitory neurons are identical; all excitatory neurons are identical.

(2) The cortex is spatially unstructured and homogeneous: Both the local and long-distance synaptic connectivities are constants that do not depend on neuron location.

(3) The abrupt nonlinear transition between quiescence and action-potential firing is represented by a population-average sigmoid [Eq. (22)] that maps from soma voltage to firing *rate*.

(4) Every neuron is buffeted by unrelenting background wash of spatiotemporal white noise [Eq. (24)].

With the inclusion of gap-junction connections, we have made additional assumptions:

(5) Via gap junctions, interneurons couple exclusively with interneurons, and excitatory neurons couple exclusively with excitatory neurons, $i-i$ coupling being stronger than $e-e$.

(6) The $i-i$ (D_2) and $e-e$ (D_1) diffusivities are uniform across the cortex.

(7) Gap-junction diffusivity is constant, independent of cortical activity [Eq. (11)]; this requires that the ratio of membrane to gap resistance, R_m/R_g, remain fixed.

(8) D_2 is large enough to destabilize the homogeneous steady state of cortical electrical activity, allowing Turing-structured patches of elevated and depressed activity to emerge spontaneously.

Assumption (7) is unlikely to be true. Typically, the effective membrane resistance is largest when the neuron is at resting potential, and decreases when either the neuron is depolarized above, or hyperpolarized below, its resting voltage. Gap-junction conductance is also known to vary as the connexin channels gate open and closed, but the general principles of junction modulation are not well understood.

The validity of assumption (8) remains an open question. As discussed in Sec. II A 4, there are new types of gap junction which are not yet fully characterized (such as pannexins, and the neuron-glial-neuron circuits), but which are likely to increase the magnitude of gap-junction effects.

C. Linking Turing structures to BOLD imagery and gamma resonances

The prediction that multiple, *separated* cortical regions can become *simultaneously* active—with intervening regions becoming inactive—is consistent with neurophysiological measurements reported by Smith *et al.* [31] and Fox *et al.* [30] of the very slow (<0.1 Hz) fluctuations in the BOLD (blood oxygen-level-dependent) signal detected using functional MRI (magnetic resonance imaging) of the human brain. The BOLD signal, being proportional to blood oxygenation, is widely used as a spatial index of neuronal activity levels. A localized positive BOLD contrast between a task and a nontask interval is taken as evidence for task-related processing in the cortical region concerned. In one experiment involving stimulation of the visual cortex, Smith *et al.* [31] found that the region of stimulation (positive BOLD) was surrounded by an extensive area of negative BOLD, indicating a reduction in neuronal activity here. In more recent work, Smith *et al.* [32] showed that the regions of negative BOLD are bracketed by regions of positive BOLD (see Fig. 3 of [32]).

The fact that our theoretical diffusive coupling strength D_2 scales with membrane resistance may have neurobiological significance: If R_m decreases with increases in firing rate, then coupling strength will diminish. This means that the Turing patterns would be expected to exchange contrast on a slow time scale, with low-firing patches increasing their activity at the expense of high-firing patches. When Fox *et al.* [30] tracked the temporal evolution of the BOLD signal during resting wakefulness, they found that widely separated brain regions participated in a synchronized, but irregular, waxing and waning of neuronal activity over periods of 10 to 30 s—i.e., a region of positive BOLD would evolve into negative BOLD and back again. Significantly, they found that these correlated patches bracketed a region whose BOLD signal oscillated in antiphase, and concluded that the brain is intrinsically organized into dynamic, anticorrelated functional networks.

The present model suggests that strong gap-junction diffusivity provides a natural mechanism for a symmetry-breaking transition that permits remote coactivation of separated neural territories. We offer the conjecture that because an activated region will have rhythmic neuronal firing patterns that are tightly correlated to gamma-frequency oscillations (20–80 Hz) in the local-field potential [33], an underlying Turing patterning would increase the probability of observing brief periods of apparently synchronized gamma oscillations. If the Turing interpretation is correct, then these fleeting cross-cortex synchronies may simply indicate that the separated regions are coactive, rather than necessarily being phase-locked or coresonant.

Narrow-band gamma synchrony has been observed by Gray *et al.* [34] at intracortical electrodes separated by 7 mm in cat visual cortex stimulated by moving light bars. Similar transient phase locking within a subset of the gamma band has been reported for pairs of scalp EEG electrodes separated by ~9 cm [35–37]. Miltner *et al.* [37] detected a significant increase in cross-electrode gamma synchrony during the 3-s *anticipation* of an electric shock to the finger (the so-called "contingent negative variation" or "readiness potential")—this duration is not too dissimilar to the ~1–1.5 s required for the development of the Turing patterns whose time courses are traced in Figs. 7(a)–7(c).

In summary, we have demonstrated that the inclusion of inhibitory diffusion in a two-dimensional mean-field cortical model can lead to the spontaneous formation of Turing patterns of high and low neural activity that extend across the cortex, thus allowing spatially separated regions to become simultaneously activated. This suggests that the formation of macroscale cortical patterns may provide an indirect measure of microscale gap-junction connection strength. We argue that the high- and low-activity Turing regions are the source of the positive (enhanced) and negative (suppressed) BOLD signal fluctuations detected in functional MRI scans, and we hypothesize that the separated regions of spontaneous cortical activation may provide a plausible neural substrate for the observation of fleeting gamma-band synchrony detected between separated EEG scalp or cortical electrodes.

ACKNOWLEDGMENTS

The area-overlap model of Appendix B arose from comments by an anonymous Referee who supplied the form of the distribution (B3) and the resulting (B8) estimate for D_2. We appreciate this assistance.

APPENDIX A: GAUSSIAN-DISTRIBUTED GAP JUNCTIONS

The Eq. (11) expression for diffusive coupling strength D_2 (derived in Sec. II A 3) assumes an idealized top-hat profile for the zone of gap-junction sensitivity surrounding the neuron of interest. We now derive the coupling strength for the case of a radially symmetric gap-junction distribution described by a Gaussian profile centered on the neuron. We note that a Gaussian function would make a plausible fit to the measurements reported by Fukuda *et al.* [26].

We consider a single neuron whose soma is located at the origin of a two-dimensional Cartesian coordinate system

with axes x and y. We define a two-dimensional probability density function $\rho(r)$, with $r^2=x^2+y^2$:

$$\rho(r) = \frac{1}{\pi\sigma^2}\exp(-r^2/\sigma^2), \tag{A1}$$

so that $\rho(r)dxdy$ denotes the probability that a given gap junction links this soma with another in a small area between x and $x+dx$, y and $y+dy$. The term σ is the root-mean-square distance for the two-dimensional Gaussian distribution: $\sigma = \sqrt{\langle r^2\rangle}$.

To compute the current that will flow into this neuron, due to the conduction of charge from other neurons through gap junctions, we integrate over all space the product of the potential at the point in space relative to that of the neuron, the probability density of connections at this point in space, the total gap junctions per neuron, and the conductance per gap junction. This gives

$$I_0 = \frac{N^\gamma}{\pi\sigma^2 R_g}\int_x\int_y [V(r)-V_0]\exp(-r^2/\sigma^2)dx\,dy, \tag{A2}$$

where N^γ is the total number of gap junctions per neuron, and R_g is the gap-junction resistance, equal to the reciprocal of the gap-junction conductance.

This flow of charge over a time Δt causes a rise in average soma potential, given by $\Delta V_0 = I_0\Delta t/C$, where C is the capacitance of the soma and the subscript "0" denotes the neuron at the origin. We relate the capacitance to the somatic time constant τ and membrane resistance R_m through $R_mC=\tau$, and so we have $\Delta V_0 = I_0R_m\Delta t/\tau$, where I_0 is given by Eq. (A2). The potential rise over a time Δt is then

$$\Delta V_0 = \frac{N^\gamma R_m}{\pi\sigma^2 R_g}\frac{\Delta t}{\tau}\int_x\int_y (V(r)-V_0)\exp(-r^2/\sigma^2)dx\,dy. \tag{A3}$$

Next, we need to deal with the variation in soma potential over the cortex surface. We must assume that the length scale for this variation is much longer than that for gap junction connections, so that we can use the second-order Taylor expansion of $V(r)$ about the origin:

$$V(r)-V_0 \approx x\left.\frac{\partial V}{\partial x}\right|_0 + y\left.\frac{\partial V}{\partial y}\right|_0 + \frac{x^2}{2}\left.\frac{\partial^2 V}{\partial x^2}\right|_0 + \frac{y^2}{2}\left.\frac{\partial^2 V}{\partial y^2}\right|_0 + xy\left.\frac{\partial^2 V}{\partial x\,\partial y}\right|_0, \tag{A4}$$

where x and y are the displacements from the origin, and the partial derivatives are evaluated at the origin. Substituting into Eq. (A3), it is clear from symmetry arguments that the x, y and xy terms must integrate to zero. This leaves us with

$$\Delta V_0 = \frac{N^\gamma R_m}{2\pi\sigma^2 R_g}\frac{\Delta t}{\tau}\left(\left.\frac{\partial^2 V}{\partial x^2}\right|_0\int_x\int_y x^2 e^{-r^2/\sigma^2}dx\,dy + \left.\frac{\partial^2 V}{\partial y^2}\right|_0\int_x\int_y y^2 e^{-r^2/\sigma^2}dx\,dy\right). \tag{A5}$$

The two integrals are identical, with each equal to $\pi\sigma^4/2$. Combining the sum of the second-order partial derivatives as the two-dimensional Laplacian $\nabla^2 V$, we have

$$\Delta V_0 = \frac{\sigma^2 N^\gamma R_m}{4R_g}\frac{\Delta t}{\tau}\nabla^2 V|_0. \tag{A6}$$

Since we can make an arbitrary choice of origin, this equation will apply for any neuron, and so we can drop the origin suffix 0. Dividing Eq. (A6) by the time-interval Δt, then taking the limit $\Delta t\to 0$, gives the partial differential equation for the soma voltage due to diffusion currents,

$$\tau\frac{\partial V}{\partial t} = \frac{\sigma^2 N^\gamma R_m}{4R_g}\nabla^2 V = D_2^{\mathrm{G}}\nabla^2 V, \tag{A7}$$

where the D_2^{G} coefficient is the diffusive coupling strength for the case of Gaussian-distributed gap-junction connectivity.

APPENDIX B: AREA-OVERLAPPED HEAVISIDE DISKS

An anonymous referee suggested an alternative derivation for the D_2 diffusion strength based on the following assumptions:

(1) The gap junctions for a given neuron are uniformly distributed over a circular disk of radius b centered at the neuron position.

(2) The probability that a given junction links the central neuron to a second neuron is proportional to the area of the overlap of the (radius b) disks of the two neurons.

(3) The area density of cells is reasonably high.

Let the first cell be centered at the origin O, and the second cell be located at a radial separation $r\le 2b$. If the circular perimeters of the two disks intersect at points P_1, P_2, then half the overlap region is given by the area of the sector OP_1P_2 minus the area of the triangle OP_1P_2:

$$\tfrac{1}{2}A(r) = b^2[\cos^{-1}(r/2b) - (r/2b)\sqrt{1-(r/2b)^2}]. \tag{B1}$$

Integrating $A(r)$ from $r=0$ to $r=2b$ through a rotation of 2π gives

$$\int_{\theta=0}^{2\pi}\int_{r=0}^{2b} A(r)r\,dr\,d\theta = \pi^2 b^4, \tag{B2}$$

the normalization for the area-overlap distribution. Combining Eqs. (B1) and (B2) gives the area-overlap probability distribution $\rho(x,y)$,

$$\rho(x,y) = H(2b-r)\frac{2}{\pi^2 b^2}[\cos^{-1}(r/2b) - (r/2b)\sqrt{1-(r/2b)^2}], \tag{B3}$$

where $r=\sqrt{x^2+y^2}$, and $H(\cdots)$ is the Heaviside unit-step function. Reworking the theory of Appendix A with Eq. (B3) replacing the Gaussian distribution of Eq. (A1), Eq. (A5) now reads

$$\tau \frac{\partial V}{\partial t} = \frac{N^\gamma R_m}{2R_g}\left(\left.\frac{\partial^2 V}{\partial x^2}\right|_0 \int_x \int_y x^2 \rho(x,y)dx\,dy + \left.\frac{\partial^2 V}{\partial y^2}\right|_0 \int_x \int_y y^2 \rho(x,y)dx\,dy \right), \tag{B4}$$

where the double integrals are evaluated in polar coordinates with $x=r\cos\theta$, $y=r\sin\theta$, e.g.,

$$\int_x \int_y x^2 \rho(x,y)dx\,dy = \int_{\theta=0}^{2\pi}\int_{r=0}^{2b} (r\cos\theta)^2 \rho(x,y) r\,dr\,d\theta = \pi \int_{r=0}^{2b} r^3 \rho(x,y)dr = \frac{b^2}{2},$$

with an identical result for the $\int\int y^2$ double integral. Thus Eq. (B4) becomes

$$\tau \frac{\partial V}{\partial t} = \frac{b^2 N^\gamma R_m}{4R_g}\nabla^2 V = D_2^{\mathrm{H}} \nabla^2 V, \tag{B5}$$

where the D_2^{H} coefficient is the diffusive coupling strength for overlapping Heaviside-weighted disks.

Comparing the coupling strengths for the top hat [Eq. (11)], the Gaussian (A7), and the Heaviside-disk (B5) gap-junction distributions,

$$D_2 = \frac{aN^\gamma}{4}\frac{R_m}{R_g} \quad \text{(top-hat)}, \tag{B6}$$

$$D_2^{\mathrm{G}} = \frac{\sigma^2 N^\gamma}{4}\frac{R_m}{R_g} \quad \text{(Gaussian)}, \tag{B7}$$

$$D_2^{\mathrm{H}} = \frac{b^2 N^\gamma}{4}\frac{R_m}{R_g} \quad \text{(Heaviside disk)} \tag{B8}$$

we see that the three forms are equivalent, with the area of the square Fukuda cell a being replaced by an "effective area" σ^2 of the Gaussian distribution (A1), and by b^2 for the overlapping-area distribution (B3). The numerical values for effective area and coupling strength for these three models are listed in Table II.

[1] C. M. Gray, Neuron **24**, 31 (1999).
[2] J. J. Wright and D. T. J. Liley, Behav. Brain Sci. **19**, 285 (1996).
[3] D. T. J. Liley, P. J. Cadusch, and J. J. Wright, in *A Continuum Theory of Electro-Cortical Activity* (California Institute of Technology, Santa Barbara, CA, 1998).
[4] P. A. Robinson, C. J. Rennie, and J. J. Wright, Phys. Rev. E **56**, 826 (1997).
[5] C. J. Rennie, J. J. Wright, and P. A. Robinson, J. Theor. Biol. **205**, 17 (2000).
[6] M. L. Steyn-Ross, D. A. Steyn-Ross, J. W. Sleigh, and D. T. J. Liley, Phys. Rev. E **60**, 7299 (1999).
[7] M. L. Steyn-Ross, D. A. Steyn-Ross, and J. W. Sleigh, Prog. Biophys. Mol. Biol. **85**, 369 (2004).
[8] M. T. Wilson, J. W. Sleigh, D. A. Steyn-Ross, and M. L. Steyn-Ross, Anesthesiology **104**, 588 (2006).
[9] M. L. Steyn-Ross, D. A. Steyn-Ross, J. W. Sleigh, and D. R. Whiting, Phys. Rev. E **68**, 021902 (2003).
[10] M. T. Wilson, M. L. Steyn-Ross, D. A. Steyn-Ross, and J. W. Sleigh, Phys. Rev. E **72**, 051910 (2005).
[11] D. A. Steyn-Ross *et al.*, J. Biol. Phys. **31**, 547 (2005).
[12] M. T. Wilson *et al.*, J. Comput. Neurosci. **21**, 243 (2006).
[13] M. L. Steyn-Ross, D. A. Steyn-Ross, J. W. Sleigh, M. T. Wilson, and L. C. Wilcocks, Phys. Rev. E **72**, 061910 (2005).
[14] P. A. Robinson, C. J. Rennie, J. J. Wright, and P. D. Bourke, Phys. Rev. E **58**, 3557 (1998).
[15] J. J. Wright, Biol. Cybern. **76**, 181 (1997).
[16] P. A. Robinson, C. J. Rennie, J. J. Wright, H. Bahramali, E. Gordon, and D. L. Rowe, Phys. Rev. E **63**, 021903 (2001).
[17] I. Bojak and D. T. J. Liley, Phys. Rev. E **71**, 041902 (2005).
[18] P. A. Robinson, C. J. Rennie, and D. L. Rowe, Phys. Rev. E **65**, 041924 (2002).
[19] M. A. Kramer, H. E. Kirsch, and A. J. Szeri, J. R. Soc., Interface **2**, 113 (2005).
[20] M. V. Bennett and R. S. Zukin, Neuron **41**, 495 (2004).
[21] M. Galarreta and S. Hestrin, Nature (London) **402**, 72 (1999).
[22] J. R. Gibson, M. Beierlein, and B. W. Conners, Nature (London) **402**, 75 (1999).
[23] G. Tamás, E. H. Buhl, A. Lörincz, and P. Somogyi, Nat. Neurosci. **403**, 366 (2000).
[24] M. Beierlein, J. R. Gibson, and B. W. Connors, Nat. Neurosci. **3**, 904 (2000).
[25] R. D. Traub *et al.*, J. Neurosci. **21**, 9478 (2001).
[26] T. Fukuda, T. Kosaka, W. Singer, and R. A. W. Galuske, J. Neurosci. **26**, 3434 (2006).
[27] A. M. Turing, Philos. Trans. R. Soc. London **237**, 37 (1952).
[28] L. Edelstein-Keshet, *Mathematical Models in Biology* (Random House, New York, 1988).
[29] L. Yang, M. Dolnik, A. M. Zhabotinsky, and I. R. Epstein, J. Chem. Phys. **117**, 7259 (2002).
[30] M. D. Fox *et al.*, Proc. Natl. Acad. Sci. U.S.A. **102**, 9673 (2005).
[31] A. T. Smith, K. D. Singh, and M. W. Greenlee, NeuroReport **11**, 271 (2000).
[32] A. T. Smith, A. L. Williams, and K. D. Singh, Hum. Brain Mapp **21**, 213 (2004).
[33] C. M. Gray and W. Singer, Proc. Natl. Acad. Sci. U.S.A. **86**, 1698 (1989).
[34] C. M. Gray, P. König, A. K. Engel, and W. Singer, Nature (London) **338**, 334 (1989).
[35] J. E. Desmedt and C. Tomberg, Neurosci. Lett. **168**, 126 (1994).
[36] E. Rodriguez *et al.*, Nature (London) **397**, 430 (1999).
[37] W. H. R. Miltner *et al.*, Nature (London) **397**, 434 (1999).

[38] C. Koch, *Biophysics of Computation: Information Processing in Single Neurons* (Oxford University Press, New York, 1999).
[39] Y. V. Panchin, J. Exp. Biol. **208**, 1415 (2005).
[40] M. T. Barbe, H. Monyer, and R. Bruzzone, Physiology **21**, 103 (2006).
[41] B. Nadarajah, D. Thomaidou, W. H. Evans, and J. G. Parnavelas, J. Comp. Neurol. **376**, 326 (1996).
[42] V. Alvarez-Maubecin, F. García-Hernández, J. T. Williams, and E. J. Van Bockstaele, J. Neurosci. **20**, 4091 (2000).
[43] D. Schmitz *et al.*, Neuron **31**, 831 (2001).
[44] B. Ermentrout, Phys. Rev. E **74**, 031918 (2006).
[45] D. T. J. Liley, P. J. Cadusch, and J. J. Wright, Neurocomputing **26-27**, 795 (1999).
[46] D. A. Steyn-Ross, M. L. Steyn-Ross, M. T. Wilson, and J. W. Sleigh, Phys. Rev. E **74**, 051920 (2006).
[47] J. J. Wright *et al.*, BioSystems **73**, 71 (2001).
[48] The two-dimensional circular convolution algorithm was written by David Young, Department of Informatics, University of Sussex, UK. His `convolve2()` code can be downloaded from MathWorks File Exchange, http://www.mathworks.com/matlabcentral/fileexchange.